

Towards Analyzing the Influence of Measurement Errors in Magnetic Resonance Imaging of Fluid Flows — Development of an Interval-Based Iteration Approach

Kristine John^a, Andreas Rauh^b,
Martin Bruschewski^a and Sven Grundmann^a

Abstract

Magnetic Resonance Imaging (MRI) provides an insight into opaque structures and does not only have a large number of applications in the field of medical examinations but also in the field of engineering. In technical applications, MRI enables a contactless measurement of the two- or three-dimensional velocity field within minutes. However, various measurement methods would benefit from an acceleration of the measurement procedure. *Compressed Sensing* is a promising method to fit this need. A random under-sampling of the sampled data points enables a significant reduction of acquisition time. As this method requires a nonlinear iterative reconstruction of unmeasured data to obtain the same data quality as for a conventional fully sampled measurement, it is essential to estimate the influence of uncertainty on the quantitative result. This paper investigates the implementation of interval arithmetic approaches with a focus on the applicability in the frame of compressed sensing techniques. These approaches are able to handle bounded uncertainty not only in the case of linear relationships between measured data and the computed outputs but also allow for solving the necessary optimality criteria for the fluid velocity reconstruction in an iterative manner under the assumption of set-valued measurement errors and bounded representations of noise.

Keywords: Magnetic Resonance Imaging, compressed sensing, uncertainty modeling, interval analysis, Krawczyk iteration

^aUniversity of Rostock, Institute of Fluid Mechanics, Albert-Einstein-Str. 2, D-18059 Rostock, Germany, E-mail: {Kristine.John,Martin.Bruschewski,Sven.Grundmann}@uni-rostock.de

^bUniversity of Rostock, Chair of Mechatronics, Justus-von-Liebig-Weg 6, D-18059 Rostock, Germany E-mail: Andreas.Rauh@uni-rostock.de

1 Introduction

Magnetic Resonance Imaging (MRI) is commonly associated with medical examinations. Moreover, this measurement method has found increasing applications in the field of fluid mechanics in the past decade. An inherent feature of MRI is the comparatively fast two- or three-dimensional data acquisition inside opaque systems. Various studies demonstrated that MRI is capable of estimating values of different flow properties quantitatively, such as velocity, temperature, Reynolds stresses, and species concentrations in technical fluid systems [3, 7].

However, possible applications of conventional MRI methods in engineering systems are limited. Conventional methods, for example, are notably prone to flow-induced errors. An approach to overcome these errors and to enable measurements in strongly turbulent flows at high flow velocities was presented in [4]. However, the main disadvantage of this method is the long acquisition time. Apart from that, even with conventional methods, the temporal resolution of MRI is comparatively low. Therefore, it is hardly possible to capture non-stationary flows. These examples show that there is a tremendous need to accelerate data acquisition of different MRI methods and — simultaneously — to capture the effect of uncertainty.

In contrast to other imaging techniques like photography or computed tomography, MRI measurements are based on determining spatial frequencies rather than measuring a spatial distribution. For that reason, the two- or three-dimensional measured data are referred to as k -space. The reconstruction of the spatial data from the frequency domain is straightforward using the discrete Fourier transform. Therefore, the size of the k -space matrix defines the resolution of the final data. At the same time, the number of sampled frequencies determines the required measurement time. Hence, an acceleration of the measurement is thus possible by measuring less spatial frequencies. However, only an approach that preserves the high resolution of the MRI measurement is favorable.

A promising method to achieve this is *Compressed Sensing* [15]. In this method, a random sampling of the spatial frequencies allows a considerable reduction of measurement time. Due to random sampling, noise-like errors occur when applying a linear reconstruction, whereas a nonlinear iterative reconstruction estimates the missing values and, therefore, undersampling errors are suppressed.

As in any other measurement technique, uncertainties due to the thermal noise of the receiver chain and external sources of errors corrupt the data. Besides, systematic errors due to flow instabilities and other flow- or imaging-related errors may occur. Some of these appear as random ghosts, which will eventually lead to difficulties in the nonlinear iterative reconstruction. Hence, it is of great interest to investigate how statistical uncertainty and measurement errors affect the results of image reconstruction in MRI when applying *Compressed Sensing*. Throughout this paper, bounded intervals represent these uncertainties and are therefore able to capture equally the effect of random noise within certain interval bounds (however, without any need to know the underlying probability distributions) or the influence of bounded systematic errors. If stochastic effects play a major role, those interval ranges need to be defined in such a way that they contain a certain percentage

of uncertain data. As shown in Sec. 5, these intervals can exemplarily be deduced from empirical standard deviations. Alternative methods to estimate these intervals (without the aim of providing a list of all reasonable options) rely either on a multiplicative inflation of each measured point in the k -space or make use of interval data that are coupled with variations of the power spectral density.

This paper is structured as follows. Sec. 2 gives an overview of the fundamental principles of MRI measurement techniques. Nonlinear least-squares techniques for the reconstruction of fluid velocities in the field of MRI are summarized in Sec. 3 before novel interval procedures are developed in Sec. 4 which allow for a quantification of uncertainty in the field of compressed sensing. Representative numerical results for a benchmark scenario comprising real measured data, acquired with the help of an MRI scanner available at the University of Rostock, are presented in Sec. 5. Finally, conclusions and an outlook on future work are given in Sec. 6.

2 Fundamentals of MRI-Based Measurements

The interaction of the nuclear spin with a strong external magnetic field and the corresponding effect of nuclear magnetic resonance (NMR) are the fundamentals of MRI. In general, MRI works on every chemical element containing a non-zero atomic spin. However, conventional MRI typically images hydrogen. A high-frequency excitation pulse and fast switching of magnet field gradients generate a complex-valued signal that provides a two- or three-dimensional insight into the measured human body or technical system. As mentioned before, the MRI data consists of the spatial frequencies from the area that is investigated; in MRI, this area is usually referred to as the Field of View (FOV). The application of the discrete Fourier transform yields a complex data set in the spatial domain, which then provides observable information that can then either be visualized or analyzed further in a quantitative manner. In this resulting data set, the magnitude indicates the signal intensity, while the image phase offers the possibility to encode other parameters such as velocity or temperature.

The final spatial resolution of the measured data is proportional to the size of the k -space. The acquisition time of an MRI measurement, in turn, depends on the number of sampled frequencies as well as on the used measurement method; in MRI, this measurement method is usually also called a *sequence*. A sequence, in general, consists of three parts: First, the excitation of the FOV takes place by using a high-frequency pulse. Afterwards, several magnetic field gradients are played out to encode location, velocity, or other information. Third, readout takes place. This procedure repeats as often as it is required to capture all spatial frequencies. Depending on the sequence design, it becomes possible to derive strategies that range from gathering measurements by sampling of a single data point up to investigating the whole k -space at once within a single repetition. Most conventional methods make use of a line-wise sampling, which results in comparatively short acquisition times and acceptable errors for most applications. However, there are various other possibilities for a sequence design. Depending on that, the different

approaches are more or less prone to several systematic errors and require a few tenths of a second up to several minutes of measurement time. In general, the more excitations are needed to complete the measurement, the more extended the acquisition time is. For more details on the nuclear physics of MRI and different sampling methods, the interested reader may refer to [2].

2.1 Velocity Measurement

In recent years, MRI gained much interest from the field of fluid mechanics, because it enables contactless measurement of velocity fields and other flow-related parameters without requiring optical access. The most successful approaches of measuring velocities with MRI make use of a phase-contrast measurement similar to the method developed in [17]. Due to multiple mechanisms that affect the image phase of the MRI signal, it is not possible to obtain the absolute velocities from the image phase ϕ of a single measurement. Therefore, capturing one velocity component requires two separate measurements with varying velocity encoding. The phase difference $\Delta\phi$ between these two complex data sets \mathbf{X}_1 and \mathbf{X}_2 results from

$$\Delta\phi = \angle(\mathbf{X}_2^* \cdot \mathbf{X}_1) \quad , \quad (1)$$

where $(\cdot)^*$ indicates the conjugate complex of the respective argument. Here, the phase angle is determined element-wise for a complex-valued quantity $x = x_R + jx_I$, $x_R \in \mathbb{R}$, $x_I \in \mathbb{R}$ with the complex unit j according to the MATLAB-like syntax $\angle(z) = \text{atan2}(x_I, x_R)$. The velocity u for each entry in the phase data set $\Delta\phi$ is computed element-wise from this data set by accounting for the predefined velocity sensitivity v_{enc} in the expression

$$u = \Delta\phi \frac{v_{\text{enc}}}{\pi} \quad . \quad (2)$$

In addition, the image magnitude provides information on the signal intensity. Because only areas containing a high amount of hydrogen enable a strong MRI signal, the values of surroundings such as air and walls are close to zero with randomly distributed phase angles. Note that a high density of hydrogen does not necessarily result in a high signal intensity. Other effects like the relaxation of the MRI signal and flow instabilities can also cause a significant signal loss. However, the image magnitude enables the segmentation of regions of interest (ROI) from the surrounding at least as if the signal to noise ratio (SNR) is sufficiently large.

One of the most important sources of noise in an MRI measurement is the thermal noise of the receiver chain. Bruschewski *et al.* [3] presented a robust calculation of the measurement uncertainty from the variance (Var) of two equally measured images A and B

$$\sigma_u = \frac{1}{\sqrt{2 \cdot n_{\text{SA}}}} \sqrt{\text{Var}\{u_A(\text{ROI}) - u_B(\text{ROI})\}} \quad , \quad (3)$$

where n_{SA} indicates the number of signal averages. Besides that, several systematic errors may occur. As every spatial frequency contains information of every pixel

inside the FOV, the MRI signal is averaged during the measurement. Especially in flow measurements, the occurrence of instabilities and turbulence will lead to small k -space changes within the data acquisition which are observable as ghosts in the final image.

Furthermore, as already mentioned, these effects reinforce signal loss, which will lead to a decrease in SNR. Additionally, the encoding process in most conventional measurement methods is not instantaneous. Encoding of location and velocity components takes place at different time steps, which eventually leads to a distortion of the geometry and the flow field, known as *misregistration* [14].

As soon as multiple measurements have been performed, a simple estimate of the accuracy is obtained by calculating the flow rate Q for each of the repetitions. In an $n \times m$ image, the flow rate results from the summed flow velocities in the region of interest $u(\text{ROI})$ and the pixel size A

$$Q = \sum_{i=1}^n \sum_{j=1}^m u_{ij}(\text{ROI}) \cdot A . \quad (4)$$

2.2 Fundamental Optimization Problem Related to Compressed Sensing

Donoho [6] and Candés *et al.* [5] first presented the mathematical approach of *Compressed Sensing* for which [15] demonstrated that this method is perfectly applicable to MRI. In general, three necessary conditions are required to apply compressed sensing: First, a random sampling pattern is required that will result in noise-like errors if applying a linear reconstruction. Second, the data must have a sparse representation in a known transform domain. Finally, iterative nonlinear reconstruction is required to obtain a data quality comparable with that of a conventional measurement. Applying this to MRI is straightforward by randomly skipping repetitions within the data acquisition, which will result in randomly missing data points in the k -space. These missing values are set to zero (*zero filling*) to obtain an initialization value for the iterative reconstruction. Second, like any other natural image, conventional MRI images have a sparse representation in a transform domain, for example, if calculating the finite differences, also known as *total variation* (TV transform) [15]. If applying this to a perfect noise-free image, only data points with high contrast will lead to high values while the rest is zero (*sparsity*). However, if randomly distributed noise and noise-like errors occur in the image, the sparse representation of the image is no longer sparse in the mathematical sense. Therefore, the iterative nonlinear reconstruction of the missing data points necessitates the sparsity-enforcing minimization of the l_1 norm $\|\cdot\|_1$ of the sparse transform Ψ of the image \mathbf{X} , i.e.,

$$\min J_2(\mathbf{x}) = \|\Psi\{\mathbf{X}\}\|_1 . \quad (5)$$

The Euclidean norm $\|\cdot\|_2$ of the deviation between the measured k -space data \mathbf{Y} and the Fourier transform $\mathcal{F}^{(2)}$ of the reconstructed image \mathbf{X} restricts the solution

domain of this optimization in terms of the constraint

$$J_1(\mathbf{x}) = \left\| \tilde{\mathbf{M}}_s \circ \mathcal{F}^{(2)}\{\mathbf{X}\} - \mathbf{Y} \right\|_2^2 < \epsilon . \quad (6)$$

The matrix $\tilde{\mathbf{M}}_s$ in (6) represents the undersampling and zero-filling utilizing the element-wise Hadamard product and ϵ defines the tolerance of the reconstruction. This optimization problem is solved in its unconstrained Lagrangian form leading to the cost function

$$\begin{aligned} J(\mathbf{x}) &= J_1(\mathbf{x}) + \lambda \cdot J_2(\mathbf{x}) \\ &= \left\| \tilde{\mathbf{M}}_s \circ \mathcal{F}^{(2)}\{\mathbf{X}\} - \mathbf{Y} \right\|_2^2 + \lambda \cdot \|\Psi\{\mathbf{X}\}\|_1 \quad \text{with } \lambda > 0 \end{aligned} \quad (7)$$

as proposed in Lustig *et al.* [15].

Holland *et al.* [10] made suggestions to extend this cost function to achieve an improved reconstruction, especially in technical phase-contrast measurements. They proposed a separated sparse transform of the real $\Re\{\cdot\}$ and imaginary $\Im\{\cdot\}$ parts of the data to prevent errors in the phase reconstruction, i.e.,

$$J_2(\mathbf{x}) = \|\Psi\{\Re\{\mathbf{X}\}\} + j\Psi\{\Im\{\mathbf{X}\}\}\|_1 . \quad (8)$$

Moreover, they suggested a further constraint of the optimization problem: As the geometry in technical MRI is commonly well known, they defined a binary mask \mathbf{M}_b which is zero at data points where no signal is expected, which can be expressed according to

$$J_3(\mathbf{x}) = \|(\mathbf{E} - \mathbf{M}_b) \circ \mathbf{X}\|_2^2 , \quad (9)$$

where \mathbf{E} is a matrix containing the value one in all of its entries and having the same dimension as the binary mask \mathbf{M}_b and the image \mathbf{X} .

Furthermore, additional sparse transforms can be used to reconstruct the undersampled data. In this paper, the cost function includes the total variation Ψ_{TV} and the Wavelet transform Ψ_W . The resulting cost function $J(\mathbf{x})$ is then defined as

$$\begin{aligned} J(\mathbf{x}) &= \left\| \tilde{\mathbf{M}}_s \circ \mathcal{F}^{(2)}\{\mathbf{X}\} - \mathbf{Y} \right\|_2^2 \\ &\quad + \lambda_1 \cdot \|\Psi_{TV}\{\Re\{\mathbf{X}\}\} + j\Psi_{TV}\{\Im\{\mathbf{X}\}\}\|_1 \\ &\quad + \lambda_2 \cdot \|\Psi_W\{\Re\{\mathbf{X}\}\} + j\Psi_W\{\Im\{\mathbf{X}\}\}\|_1 \\ &\quad + \lambda_3 \cdot \|(\mathbf{E} - \mathbf{M}_b) \circ \mathbf{X}\|_2^2 . \end{aligned} \quad (10)$$

Details concerning the actual choice of the total variation term as well as the Wavelet transform as regularizing and sparsity-enforcing cost function components are given in Sec. 3.3.

3 Nonlinear Least-Squares Estimation Techniques for the Reconstruction of Fluid Velocities from Undersampled k -Space Measurements

The fully sampled k -space (\mathbf{Y}) is transformed back to the original image space by applying the two-dimensional inverse Fourier transform. The definition of the (normalized) standard one-dimensional discrete Fourier transform of the data set \mathbf{X} is

$$\mathcal{F}\{\mathbf{X}\} = \mathbf{F}(\mathbf{X}) \quad \text{with } \mathbf{X} \in \mathbb{C}^{m \times n} \text{ ,} \quad (11)$$

which is applied in a column-wise manner to the data \mathbf{X} given in matrix form. The two-fold application of this one-dimensional transform then expresses the two-dimensional discrete Fourier transform $\mathcal{F}^{(2)}\{\mathbf{X}\}$:

$$\mathcal{F}^{(2)}\{\mathbf{X}\} = \mathbf{F}^{(2)}(\mathbf{X}) = \mathcal{F}\left\{\mathcal{F}\{\mathbf{X}\}^T\right\}^T \quad \text{with } \mathbf{X} \in \mathbb{C}^{m \times n} \text{ .} \quad (12)$$

This can be stated analogously in terms of the complex-valued matrix product [9, 20, 21, 24]

$$\mathcal{F}^{(2)}\{\mathbf{X}\} = \mathbf{W}_1 \cdot \mathbf{X} \cdot \mathbf{W}_2^T \text{ ,} \quad (13)$$

Here, the matrices \mathbf{W}_1 and \mathbf{W}_2 result from the application of the one-dimensional Fourier transform to the square identity matrices $\mathbf{I}_m \in \mathbb{R}^{m \times m}$ and $\mathbf{I}_n \in \mathbb{R}^{n \times n}$ according to

$$\mathbf{W}_1 = \mathcal{F}\{\mathbf{I}_m\} \quad \text{and} \quad \mathbf{W}_2 = \mathcal{F}\{\mathbf{I}_n\} \text{ .} \quad (14)$$

Due to the before-mentioned normalization of the Fourier transform operator $\mathcal{F}\{\mathbf{X}\}$, the inverse of the matrices \mathbf{W}_1 and \mathbf{W}_2 is given by

$$\mathbf{W}_1^{-1} = \mathbf{W}_1^H = (\mathbf{W}_1^*)^T \quad \text{and} \quad \mathbf{W}_2^{-1} = \mathbf{W}_2^H = (\mathbf{W}_2^*)^T \text{ ,} \quad (15)$$

where the operator $(\cdot)^*$ as also in (1) represents the conjugate complex, and $(\cdot)^H$ is the Hermitian (conjugate complex and transposed) of the respective argument. Taking into account the information given above in Eqs. (11)–(14), a column-wise notation of the two-dimensional Fourier transform, making use of the Kronecker matrix product [25] of \mathbf{W}_2 and \mathbf{W}_1 , leads to

$$\text{col}\left(\mathcal{F}^{(2)}\{\mathbf{X}\}\right) = \text{col}\left(\mathbf{W}_1 \cdot \mathbf{X} \cdot \mathbf{W}_2^T\right) = (\mathbf{W}_2 \otimes \mathbf{W}_1) \cdot \mathbf{x} \quad (16)$$

with the matrix argument \mathbf{X} reshaped into the column vector

$$\mathbf{x} = \text{col}(\mathbf{X}) \in \mathbb{C}^{m \cdot n \times 1} \text{ .} \quad (17)$$

Hence, the partial derivative of (16) with respect to the image \mathbf{X} in column-wise notation is given by

$$\frac{\partial\left(\text{col}\left(\mathcal{F}^{(2)}\{\mathbf{X}\}\right)\right)}{\partial \mathbf{x}} = \mathbf{W}_2 \otimes \mathbf{W}_1 \text{ .} \quad (18)$$

This partial derivative will be exploited later on in order to derive necessary optimality criteria for the reconstruction of the image \mathbf{X} from undersampled measured data \mathbf{Y} by minimizing the cost function (10). In analogy to the reconstructed image, the application of the column operator to the undersampled measured data set yields

$$\mathbf{y} = \text{col}(\mathbf{Y}) . \quad (19)$$

Furthermore, denote $\mathbf{y}' \in \mathbb{C}^{N'}$, $N' \leq m \cdot n$, as the vector of measured data from which all zero-elements resulting from zero-filling are removed.

3.1 Fundamental Least-Squares Optimization Problem

Under consideration of these preliminaries, the term $J_1(\mathbf{x})$ of the cost function $J(\mathbf{x})$ derived in (10) can be formulated according to

$$\begin{aligned} J_1(\mathbf{x}) &= \left\| \tilde{\mathbf{M}}_s \circ \mathcal{F}^{(2)} \{ \mathbf{X} \} - \mathbf{Y} \right\|_2^2 \\ &= \left(\mathbf{M}_s \cdot (\mathbf{W}_2 \otimes \mathbf{W}_1) \cdot \mathbf{x} - \mathbf{y}' \right)^H \cdot \left(\mathbf{M}_s \cdot (\mathbf{W}_2 \otimes \mathbf{W}_1) \cdot \mathbf{x} - \mathbf{y}' \right) \\ &= \left(\mathbf{M}_s \cdot (\mathbf{W}_2 \otimes \mathbf{W}_1)^* \cdot \mathbf{x}^* - \mathbf{y}'^* \right)^T \cdot \left(\mathbf{M}_s \cdot (\mathbf{W}_2 \otimes \mathbf{W}_1) \cdot \mathbf{x} - \mathbf{y}' \right) , \end{aligned} \quad (20)$$

with \mathbf{M}_s as a substitute for $\tilde{\mathbf{M}}_s$ in classical matrix-vector multiplication. Now, necessary optimality criteria are derived subsequently for the unconstrained minimization of the cost function (20) by a suitable choice of the complex-valued vector \mathbf{x} .

3.1.1 Analysis of Complex Differentiability

Before the necessary optimality criterion for the reconstruction of \mathbf{x} can be stated, differentiability of $J_1(\mathbf{x})$ with respect to the complex-valued argument \mathbf{x} needs to be analyzed. Generally, the cost function $J_1(\mathbf{x})$ can be split up into its real and imaginary parts according to

$$J_1(\mathbf{x}) = U(\mathbf{x}_R, \mathbf{x}_I) + jV(\mathbf{x}_R, \mathbf{x}_I) \quad (21)$$

with the respective arguments $\mathbf{x}_R = \text{col}(\Re \{ \mathbf{X} \})$ and $\mathbf{x}_I = \text{col}(\Im \{ \mathbf{X} \})$, i.e., $\mathbf{x} = \mathbf{x}_R + j\mathbf{x}_I$.

Note that due to the fact that the cost function $J_1(\mathbf{x})$ is defined as the square of the magnitude of a complex-valued vector argument, the relation

$$V(\mathbf{x}_R, \mathbf{x}_I) = 0 \quad (22)$$

holds true for arbitrary arguments $\mathbf{x} = \mathbf{x}_R + j\mathbf{x}_I$. Classically, necessary optimality criteria for regular extrema of a cost function $J_1(\mathbf{x})$ are determined by computing the first partial derivative with respect to its argument and setting the resulting vector to zero. For complex-valued arguments such kind of differentiation in the

classical sense, i.e., the kind of differentiation rules that are well-known for real-valued functions with real arguments, is only possible in a straightforward manner if the Cauchy-Riemann equations [11]

$$\frac{\partial U(\mathbf{x}_R, \mathbf{x}_I)}{\partial \mathbf{x}_R} = \frac{\partial V(\mathbf{x}_R, \mathbf{x}_I)}{\partial \mathbf{x}_I} \quad \text{and} \quad \frac{\partial U(\mathbf{x}_R, \mathbf{x}_I)}{\partial \mathbf{x}_I} = -\frac{\partial V(\mathbf{x}_R, \mathbf{x}_I)}{\partial \mathbf{x}_R} \quad (23)$$

are satisfied. However, this is never true for quadratic vector norms such as (20) as well as for the absolute value of a complex argument. This statement is easily verified by the fact that

$$\frac{\partial V(\mathbf{x}_R, \mathbf{x}_I)}{\partial \mathbf{x}_R} \equiv \mathbf{0} \quad \text{and} \quad \frac{\partial V(\mathbf{x}_R, \mathbf{x}_I)}{\partial \mathbf{x}_I} \equiv \mathbf{0} \quad (24)$$

hold true because possible function values of $J_1(\mathbf{x})$ are always real and non-negative. Hence, the cost function $J_1(\mathbf{x})$ is proven not to be an analytic function for arbitrary complex vector arguments \mathbf{x} [1, 8].

Therefore, $J_1(\mathbf{x})$ needs to be considered as a bi-variate function in both vector arguments \mathbf{x}_R and \mathbf{x}_I [1, 8]. Then, the total differential dJ_1 with respect to both independent arguments is computed according to

$$dJ_1 = \frac{\partial J_1(\mathbf{x}_R, \mathbf{x}_I)}{\partial \mathbf{x}_R} d\mathbf{x}_R + \frac{\partial J_1(\mathbf{x}_R, \mathbf{x}_I)}{\partial \mathbf{x}_I} d\mathbf{x}_I \quad (25)$$

with the independent differentials $d\mathbf{x}$ and $d\mathbf{x}^*$ for \mathbf{x} and its conjugate complex \mathbf{x}^* , respectively, which are given by

$$\begin{aligned} d\mathbf{x} &= d\mathbf{x}_R + j d\mathbf{x}_I \quad \text{and} \\ d\mathbf{x}^* &= d\mathbf{x}_R - j d\mathbf{x}_I . \end{aligned} \quad (26)$$

Using those independent differentials, the Wirtinger differential operators (cf. [1, 8, 11]) can be defined for which the classical rules for differentiation hold according to the well-known rules for differentiation of real-valued functions with real arguments:

$$\begin{aligned} \frac{\partial}{\partial \mathbf{x}} &:= \frac{1}{2} \cdot \left(\frac{\partial}{\partial \mathbf{x}_R} - j \frac{\partial}{\partial \mathbf{x}_I} \right) \quad \text{and} \\ \frac{\partial}{\partial \mathbf{x}^*} &:= \frac{1}{2} \cdot \left(\frac{\partial}{\partial \mathbf{x}_R} + j \frac{\partial}{\partial \mathbf{x}_I} \right) , \quad \text{respectively} . \end{aligned} \quad (27)$$

3.1.2 Derivation of Necessary Optimality Criteria

Using the differentials (27), the total differential of the cost function term $J_1(\mathbf{x})$ under consideration is given by

$$dJ_1 = \left(\frac{\partial J_1}{\partial \mathbf{x}} \right)^T \cdot d\mathbf{x} + \left(\frac{\partial J_1}{\partial \mathbf{x}^*} \right)^T \cdot d\mathbf{x}^* \quad (28)$$

with

$$\frac{\partial J_1}{\partial \mathbf{x}} = \left(\mathbf{M}_s \cdot (\mathbf{W}_2 \otimes \mathbf{W}_1) \right)^T \cdot \left(\mathbf{M}_s \cdot (\mathbf{W}_2 \otimes \mathbf{W}_1)^* \cdot \mathbf{x}^* - \mathbf{y}'^* \right) \quad (29)$$

as well as

$$\frac{\partial J_1}{\partial \mathbf{x}^*} = \left(\mathbf{M}_s \cdot (\mathbf{W}_2 \otimes \mathbf{W}_1)^* \right)^T \cdot \left(\mathbf{M}_s \cdot (\mathbf{W}_2 \otimes \mathbf{W}_1) \cdot \mathbf{x} - \mathbf{y}' \right) . \quad (30)$$

A thorough analysis of the expressions (29) and (30) shows that

$$\frac{\partial J_1}{\partial \mathbf{x}^*} = \left(\frac{\partial J_1}{\partial \mathbf{x}} \right)^* \quad (31)$$

always holds for the cost function under investigation. Therefore, differentiation with respect to both \mathbf{x} and \mathbf{x}^* and setting the total differential dJ_1 in (28) to zero yields the unique optimum (in the least-squares sense) specified by the algebraic set of equations

$$\frac{\partial J_1}{\partial \mathbf{x}^*} = \mathbf{0} . \quad (32)$$

Due to the underdetermined nature of the expression $\mathbf{M}_s \cdot (\mathbf{W}_2 \otimes \mathbf{W}_1) \cdot \mathbf{x} - \mathbf{y}' = \mathbf{0}$, it is replaced by the minimum norm solution

$$\mathbf{x}_{\text{opt}} = \mathcal{M}_s^+ \cdot \mathbf{y}' , \quad (33)$$

where uniqueness of \mathbf{x}_{opt} is ensured if the matrix

$$\mathcal{M}_s = \mathbf{M}_s \cdot (\mathbf{W}_2 \otimes \mathbf{W}_1) \quad (34)$$

has full rank¹ and hence its left pseudo inverse

$$\mathcal{M}_s^+ = \left(\mathcal{M}_s^{*T} \cdot \mathcal{M}_s \right)^{-1} \cdot \mathcal{M}_s^{*T} \quad (35)$$

exists. For the image reconstruction by means of the fully sampled k -space, \mathbf{M}_s becomes equal to the identity matrix of appropriate dimension and hence, \mathcal{M}_s^+ turns into the operator of the exact inverse of the two-dimensional Fourier transformation (13) and (16).

3.2 Extended Least-Squares Optimization Problem

Now, the derivation of necessary optimality criteria for the minimization of the overall cost function (10) is continued. To achieve differentiability of this cost function according to (28)–(32), it is approximated by the following expression

$$\begin{aligned} J(\mathbf{x}) \approx & \left\| \mathbf{M}_s \cdot (\mathbf{W}_2 \otimes \mathbf{W}_1) \cdot \mathbf{x} - \mathbf{y}' \right\|_2^2 + \lambda_1 \cdot \sqrt{\left\| \Psi_{\text{TV}} \cdot \mathbf{x} \right\|_2^2 + \mu_{\text{TV}}} \\ & + \lambda_2 \cdot \sqrt{\left\| \Psi_{\text{W}} \cdot \mathbf{x} \right\|_2^2 + \mu_{\text{W}}} + \lambda_3 \cdot \left\| (\mathbf{E} - \mathbf{M}_b) \circ \mathbf{X} \right\|_2^2 \end{aligned} \quad (36)$$

¹Note that the full rank property of the matrix (34) corresponds to strict positive definiteness of the cost function $J_1(\mathbf{x})$ defined in (20).

with the sufficiently small regularization parameters $\mu_\iota > 0$, $\iota \in \{\text{TV}, \text{W}\}$.

Applying the Wirtinger differentials (27) to the purely quadratic term

$$Q_1(\mathbf{x}) = J_1(\mathbf{x}) = \|\mathbf{M}_s \cdot (\mathbf{W}_2 \otimes \mathbf{W}_1) \cdot \mathbf{x} - \mathbf{y}'\|_2^2 \quad (37)$$

with the complex-valued vector argument $\mathbf{M}_s \cdot (\mathbf{W}_2 \otimes \mathbf{W}_1) \cdot \mathbf{x} - \mathbf{y}' \in \mathbb{C}^{N'}$ leads to the partial derivatives

$$\begin{aligned} \frac{\partial Q_1(\mathbf{x})}{\partial \mathbf{x}} &= (\mathbf{M}_s \cdot (\mathbf{W}_2 \otimes \mathbf{W}_1))^T \cdot (\mathbf{M}_s \cdot (\mathbf{W}_2 \otimes \mathbf{W}_1)^* \cdot \mathbf{x}^* - \mathbf{y}'^*) \quad \text{and} \\ \mathbf{f}_1(\mathbf{x}) := \frac{\partial Q_1(\mathbf{x})}{\partial \mathbf{x}^*} &= (\mathbf{M}_s \cdot (\mathbf{W}_2 \otimes \mathbf{W}_1)^*)^T \cdot (\mathbf{M}_s \cdot (\mathbf{W}_2 \otimes \mathbf{W}_1) \cdot \mathbf{x} - \mathbf{y}') \quad . \end{aligned} \quad (38)$$

Analogously, the square root expressions in (36) (representing the regularization of the l_1 norm expressions given by the second and third summands in the cost function (10)) can be redefined as

$$Q_\iota(\mathbf{x}) = \sqrt{\|\Psi_\iota \cdot \mathbf{x}\|_2^2 + \mu_\iota} = \sqrt{\mathbf{x}^{*T} \cdot \Psi_\iota^{*T} \cdot \Psi_\iota \cdot \mathbf{x} + \mu_\iota} \quad , \quad \iota \in \{\text{TV}, \text{W}\} \quad , \quad (39)$$

with the corresponding derivatives

$$\frac{\partial Q_\iota(\mathbf{x})}{\partial \mathbf{x}} = \frac{\Psi_\iota^T \cdot \Psi_\iota^* \cdot \mathbf{x}^*}{2Q_\iota(\mathbf{x})} \quad \text{and} \quad \mathbf{f}_\iota(\mathbf{x}) := \frac{\partial Q_\iota(\mathbf{x})}{\partial \mathbf{x}^*} = \frac{\Psi_\iota^{*T} \cdot \Psi_\iota \cdot \mathbf{x}}{2Q_\iota(\mathbf{x})} \quad . \quad (40)$$

Finally, the term

$$\begin{aligned} Q_{\text{Mb}}(\mathbf{x}) &= \|(\mathbf{E} - \mathbf{M}_b) \circ \mathbf{X}\|_2^2 \\ &= \text{col}((\mathbf{E} - \mathbf{M}_b) \circ \mathbf{X}^*)^T \cdot \text{col}((\mathbf{E} - \mathbf{M}_b) \circ \mathbf{X}) \\ &= \mathbf{x}^{*T} \cdot \text{diag}\{\text{col}(\mathbf{E} - \mathbf{M}_b)\}^T \cdot \text{diag}\{\text{col}(\mathbf{E} - \mathbf{M}_b)\} \cdot \mathbf{x} \\ &= \mathbf{x}^{*T} \cdot \text{diag}\{\text{col}(\mathbf{E} - \mathbf{M}_b)\} \cdot \mathbf{x} \end{aligned} \quad (41)$$

is also re-written in terms of a quadratic form in the complex vector argument \mathbf{x} , where $\text{diag}\{\text{col}(\mathbf{E} - \mathbf{M}_b)\}$ denotes a diagonal matrix formed by the elements of the vector $\text{col}(\mathbf{E} - \mathbf{M}_b)$. Hence, the associated derivatives are given by

$$\begin{aligned} \frac{\partial Q_{\text{Mb}}(\mathbf{x})}{\partial \mathbf{x}} &= \text{diag}\{\text{col}(\mathbf{E} - \mathbf{M}_b)\} \cdot \mathbf{x}^* =: \mathcal{M}_b \cdot \mathbf{x}^* \quad \text{and} \\ \mathbf{f}_{\text{Mb}}(\mathbf{x}) := \frac{\partial Q_{\text{Mb}}(\mathbf{x})}{\partial \mathbf{x}^*} &= \text{diag}\{\text{col}(\mathbf{E} - \mathbf{M}_b)\} \cdot \mathbf{x} =: \mathcal{M}_b \cdot \mathbf{x} \quad . \end{aligned} \quad (42)$$

The partial derivatives specified in (38), (40), and (42) can now be used to formulate a generalization of the expressions (31) and (32) according to

$$\begin{aligned} \frac{\partial J(\mathbf{x})}{\partial \mathbf{x}^*} &= \left(\frac{\partial J(\mathbf{x})}{\partial \mathbf{x}} \right)^* \\ &= \frac{\partial Q_1(\mathbf{x})}{\partial \mathbf{x}^*} + \lambda_1 \cdot \frac{\partial Q_{\text{TV}}(\mathbf{x})}{\partial \mathbf{x}^*} + \lambda_2 \cdot \frac{\partial Q_{\text{W}}(\mathbf{x})}{\partial \mathbf{x}^*} + \lambda_3 \cdot \frac{\partial Q_{\text{Mb}}(\mathbf{x})}{\partial \mathbf{x}^*} = \mathbf{0} \quad . \end{aligned} \quad (43)$$

As before, see eq. (32), the system of algebraic equations

$$\begin{aligned} \mathbf{f}(\mathbf{x}) &= \frac{\partial J(\mathbf{x})}{\partial \mathbf{x}^*} \\ &= \mathbf{f}_1(\mathbf{x}) + \lambda_1 \cdot \mathbf{f}_{\text{TV}}(\mathbf{x}) + \lambda_2 \cdot \mathbf{f}_W(\mathbf{x}) + \lambda_3 \cdot \mathbf{f}_{\text{Mb}}(\mathbf{x}) = \mathbf{0} \end{aligned} \quad (44)$$

is solved to find the optimal solution \mathbf{x}_{opt} minimizing the cost function $J(\mathbf{x})$ in terms of its approximation in (36). However, in contrast to (32), this expression is no longer linear. Therefore, iterative solution approaches have to be employed to find appropriate values for the vector \mathbf{x} . Classically, the evaluation of this necessary optimality condition is replaced with a direct minimization of $J(\mathbf{x})$ by means of local optimization procedures such as the conjugate gradient technique. Unfortunately, such local optimization procedures do not allow for a straightforward consideration of (bounded) measurement errors in \mathbf{y} and \mathbf{y}' , respectively, and typically become less effective for increasing dimensions of the search space.

3.3 Specification of the TV-Part in the Cost Function in Matrix-Vector Form

To determine a closed-form expression for the TV operator as in (39), the upper bi-diagonal Toeplitz matrix

$$\mathbf{B}_\xi(a, b) = \begin{bmatrix} a & b & 0 & \cdots & 0 \\ 0 & a & b & \ddots & \vdots \\ \vdots & \ddots & \ddots & \ddots & 0 \\ & & \ddots & a & b \\ 0 & \cdots & & 0 & a \end{bmatrix} \in \mathbb{R}^{\xi \times \xi} \quad (45)$$

is defined. Using this matrix, the two-dimensional finite difference operator $\Psi_{\text{TV}} \cdot \mathbf{x}$ can be expressed according to

$$\begin{aligned} \Psi_{\text{TV}} \cdot \mathbf{x} &= \text{col}(\mathbf{T}_m \cdot \mathbf{X}) + \text{col}((\mathbf{T}_n \cdot \mathbf{X}^T)^T) \\ &= ((\mathbf{I}_n \otimes \mathbf{T}_m) + (\mathbf{T}_n \otimes \mathbf{I}_m)) \cdot \mathbf{x} . \end{aligned} \quad (46)$$

Here, the reformulation of the column operators $\text{col}(\cdot)$ exploits the general property [25]

$$\text{col}(\mathbf{A} \cdot \mathbf{B} \cdot \mathbf{C}) = (\mathbf{I}_n \otimes (\mathbf{A} \cdot \mathbf{B})) \cdot \text{col}(\mathbf{C}) , \quad (47)$$

which is well known in the field of matrix Kronecker products, with the general matrices $\mathbf{A} \in \mathbb{R}^{k \times l}$, $\mathbf{B} \in \mathbb{R}^{l \times m}$, $\mathbf{C} \in \mathbb{R}^{m \times n}$, and the identity matrix $\mathbf{I}_n \in \mathbb{R}^{n \times n}$. Moreover, using the Toeplitz matrices $\mathbf{B}_\xi(-1, 1)$ given in (45), the matrices \mathbf{T}_ξ with $\xi \in \{m, n\}$ are defined as

$$\mathbf{T}_\xi = \begin{bmatrix} \mathbf{B}_{\xi-1}(-1, 1) & \mathbf{e}_{\xi-1} \\ \mathbf{0}_{\xi-1}^T & 0 \end{bmatrix} , \quad (48)$$

where $\mathbf{e}_{\xi-1} \in \mathbb{R}^{\xi-1}$ is the $(\xi - 1)$ th unit vector and $\mathbf{0}_{\xi-1}$ a zero vector of the specified dimension. Note, the derivation given above for the finite difference operator shows that

$$\Psi_{\text{TV}} = \Psi_{\text{TV}}^* \quad (49)$$

holds during all solution stages of the interval arithmetic solution procedures summarized in the following section.

In a similar fashion, general Wavelet transformation approaches can be restated as complex-valued matrix-vector products $\Psi_{\text{W}} \cdot \mathbf{x}$. Specifically, the square root of a quadratic norm operator over the reconstructed image according to

$$\Psi_{\text{W}} \cdot \mathbf{x} = \text{col}(\mathbf{I}_m \cdot \mathbf{X}) = (\mathbf{I}_n \otimes \mathbf{I}_m) \cdot \mathbf{x} \quad (50)$$

can be integrated at this point as the simplest version of the W-part of the cost function. Analogously, also the following simple uniform averaging operator over the reconstructed image can be expressed according to

$$\begin{aligned} \Psi_{\text{W}} \cdot \mathbf{x} &= \text{col}(\mathbf{E}_m \cdot \mathbf{X}) + \text{col}\left((\mathbf{E}_n \cdot \mathbf{X}^T)^T\right) \\ &= \left((\mathbf{I}_n \otimes \mathbf{E}_m) + (\mathbf{E}_n \otimes \mathbf{I}_m)\right) \cdot \mathbf{x} \end{aligned} \quad (51)$$

with the square matrices $\mathbf{E}_m \in \mathbb{R}^{m \times m}$ and $\mathbf{E}_n \in \mathbb{R}^{n \times n}$ containing the value one in all of their entries.

4 Interval Methods for Solving Necessary Optimality Criteria with Applications to Compressed Sensing

In this section, two possibilities are introduced for solving the nonlinear system of equations (44) by means of two different interval arithmetic approaches. The first one, which is in the focus of this paper, is a computationally less expensive approximation technique for determining confidence bounds on the reconstructed data \mathbf{x} by applying a linearized version of (44). This linearized model is then combined with an interpretation of the influence of all nonlinear terms in (44) due to (39) and (40) by additive outer interval bounds.

From that perspective, this approach can be seen as a simplified approximation of the second alternative for solving (44), namely, the Krawczyk method. This method represents an interval extension of the classical Newton iteration for finding guaranteed outer enclosures of the zeros of a nonlinear system of equations.

In contrast to the first approach, linearization errors (as well as errors due to the use of an approximate matrix inverse) are directly quantified by the Krawczyk iteration in the form of guaranteed interval bounds. Therefore, the reliability of the results is enhanced in the second alternative, on the cost of a computationally more demanding solution procedure.

4.1 An Interval-Based Linearization Technique

For the derivation of the interval-based linearization technique, the necessary optimality criterion (44) is re-written into the form

$$\left(\mathcal{M}_s^H \cdot \mathcal{M}_s + \lambda_3 \cdot \mathcal{M}_b\right) \cdot \mathbf{x} = \mathcal{M}_s^H \cdot \mathbf{y}' - \left(\lambda_1 \cdot \mathbf{f}_{TV}(\mathbf{x}) + \lambda_2 \cdot \mathbf{f}_W(\mathbf{x})\right) . \quad (52)$$

By simple algebraic reformulations, the desired result can be separated on the left-hand side of (52) according to

$$\begin{aligned} \mathbf{x} &= \left(\mathcal{M}_s^H \cdot \mathcal{M}_s + \lambda_3 \cdot \mathcal{M}_b\right)^{-1} \cdot \mathcal{M}_s^H \cdot \mathbf{y}' \\ &\quad - \left(\mathcal{M}_s^H \cdot \mathcal{M}_s + \lambda_3 \cdot \mathcal{M}_b\right)^{-1} \cdot \left(\lambda_1 \cdot \mathbf{f}_{TV}(\mathbf{x}) + \lambda_2 \cdot \mathbf{f}_W(\mathbf{x})\right) . \end{aligned} \quad (53)$$

Due to the fact that the right-hand side of (53) also depends on the unknown vector \mathbf{x} , the iterative solution process

$$\begin{aligned} [\mathbf{x}]^{(\kappa+1)} &= \left(\mathcal{M}_s^H \cdot \mathcal{M}_s + \lambda_3 \cdot \mathcal{M}_b\right)^{-1} \cdot \mathcal{M}_s^H \cdot [\mathbf{y}'] \\ &\quad - \left(\mathcal{M}_s^H \cdot \mathcal{M}_s + \lambda_3 \cdot \mathcal{M}_b\right)^{-1} \cdot \left(\lambda_1 \cdot \mathbf{f}_{TV}\left([\mathbf{x}]^{(\kappa)}\right) + \lambda_2 \cdot \mathbf{f}_W\left([\mathbf{x}]^{(\kappa)}\right)\right) \end{aligned} \quad (54)$$

is used to determine enclosures $[\mathbf{x}]$ for the image to be reconstructed.

By applying the Neumann series

$$(\mathbf{I} - \mathbf{T})^{-1} = \sum_{k=0}^{\infty} \mathbf{T}^k , \quad (55)$$

which converges if $\|\mathbf{T}^n\| < 1$ can be proven for some $n \geq 1$, and truncating the series after its linear term, the matrix inverse involved in the expression (54) can be approximated by

$$\left(\mathcal{M}_s^H \cdot \mathcal{M}_s + \lambda_3 \cdot \mathcal{M}_b\right)^{-1} \approx \mathbb{M}_{sb} := 2 \cdot \mathbf{I}_{m \cdot n} - \mathcal{M}_s^H \cdot \mathcal{M}_s - \lambda_3 \cdot \mathcal{M}_b . \quad (56)$$

This approximation avoids numerical problems of finding the exact matrix inverse due to the usually large dimensions $(m \cdot n) \times (m \cdot n)$ of the involved operands. Moreover, the numerical burden required to determine this approximation is by far smaller than computing the inverse. Note that the expression (56) holds with the equality sign for the case $\lambda_3 = 0$ (see the definition of the matrix pseudo inverse in eq. (35)). By means of numerical tests of the approximated iteration process

$$[\mathbf{x}]^{(\kappa+1)} = \mathbb{M}_{sb} \cdot \mathcal{M}_s^H \cdot [\mathbf{y}'] - \mathbb{M}_{sb} \cdot \left(\lambda_1 \cdot \mathbf{f}_{TV}\left([\mathbf{x}]^{(\kappa)}\right) + \lambda_2 \cdot \mathbf{f}_W\left([\mathbf{x}]^{(\kappa)}\right)\right) \quad (57)$$

according to Sec. 5.2, it can be shown that its outcome is sufficiently accurate in practice if it is applied to measured data with sufficiently small positive parameter values λ_3 .

The iteration (57) is initialized with the solution $[\mathbf{x}]^{(0)}$ which corresponds to setting $\lambda_1 = \lambda_2 = 0$. It is continued until it converges to a solution satisfying the element-wise enclosure property

$$[\mathbf{x}]^{(\kappa+1)} \subseteq [\mathbf{x}]^{(\kappa)} \quad \text{with} \quad \left\| \text{diam} \{ [\mathbf{x}]^{(\kappa+1)} \} - \text{diam} \{ [\mathbf{x}]^{(\kappa)} \} \right\|_2^2 < \epsilon, \quad (58)$$

where $\text{diam} \{ \cdot \}$ is the element-wise defined diameter of an interval matrix, cf. [12], and $\epsilon > 0$ a user-defined accuracy level.

To avoid the well-known problem of overestimation due to multiple dependencies of $\mathbf{f}_{\text{TV}}([\mathbf{x}]^{(\kappa)})$ and $\mathbf{f}_{\text{W}}([\mathbf{x}]^{(\kappa)})$ on common interval variables, the following range constraints can be applied during the interval evaluations of both terms $\mathbf{f}_\ell([\mathbf{x}]^{(\kappa)})$ with $\ell \in \{\text{TV}, \text{W}\}$. Analyzing the definitions (39) and (40), the complex-valued intersection relation

$$\mathbf{f}_\ell([\mathbf{x}]^{(\kappa)}) := \frac{\Psi_\ell^{*T}}{2} \cdot \check{\mathbf{f}}_\ell([\mathbf{x}]^{(\kappa)}) \quad \text{with} \quad \check{\mathbf{f}}_\ell([\mathbf{x}]^{(\kappa)}) := \left\{ \frac{\Psi_\ell \cdot [\mathbf{x}]^{(\kappa)}}{Q_\ell([\mathbf{x}]^{(\kappa)})} \cap \langle 0, \mathbf{d}_\ell^{(\kappa)} \rangle \right\} \quad (59)$$

can be defined. In (59), the first term in curly brackets denotes the naive interval evaluation of the fraction included in (40), while $\langle 0, \mathbf{d}_\ell^{(\kappa)} \rangle$ is a complex-valued interval vector in midpoint-radius notation with discs of arbitrary phase each centered at the origin of the complex plane. Each interval vector component has a radius according to its respective entry in the vector $\mathbf{d}_\ell^{(\kappa)}$, where the individual elements $(\mathbf{d}_\ell^{(\kappa)})_j \leq 1$ are determined by the following range bounds

$$\sup \left\{ \sqrt{\left\| \frac{(\Psi_\ell \cdot [\mathbf{x}]^{(\kappa)})_j}{Q_\ell([\mathbf{x}]^{(\kappa)})} \right\|_2^2} \right\} \leq (\mathbf{d}_\ell^{(\kappa)})_j \quad (60)$$

with

$$(\mathbf{d}_\ell^{(\kappa)})_j = \begin{cases} \sup \left\{ \left(\frac{\sum_{\substack{\zeta=1 \\ \zeta \neq j}}^{m \cdot n} \left(\left\| \Psi_\ell \cdot [\mathbf{x}]^{(\kappa)} \right\|_2^2 \right)_\zeta}{\left(\left\| \Psi_\ell \cdot [\mathbf{x}]^{(\kappa)} \right\|_2^2 \right)_j} \right)^{-\frac{1}{2}} \right\} < 1 \text{ for } 0 \notin \left(\left\| \Psi_\ell \cdot [\mathbf{x}]^{(\kappa)} \right\|_2^2 \right)_j \\ 1 \text{ else .} \end{cases} \quad (61)$$

Note that these range bounds can be determined in a straightforward manner by applying the triangle inequality individually to each element of (60) and overbounding the range by neglecting the positive parameter μ_ℓ in (61).

4.2 Krawczyk Iteration for an Interval-Based Solution of the Necessary Optimality Criterion

Like for the first option, this second alternative has the advantage — in contrast to local optimization procedures — that interval uncertainty in the vector \mathbf{y}' of measured data can directly be accounted for when determining interval enclosures of all possible candidates satisfying the necessary optimality condition (44). However, this second approach is a fully verified version which is not influenced by linearization errors as introduced in (56).

For that purpose, the Krawczyk operator [12, 13, 16, 18]

$$[\mathbf{k}] := \mathbf{x}_m - \mathbf{Y}_H \cdot \mathbf{f}(\mathbf{x}_m) + \left(\mathbf{I} - \mathbf{Y}_H \cdot \mathbf{H}([\mathbf{x}]) \right) \cdot ([\mathbf{x}] - \mathbf{x}_m) \quad (62)$$

needs to be evaluated in order to find a guaranteed outer interval enclosure for the complex-valued image reconstruction according to $\mathbf{x} \in [\mathbf{x}]$. This iterative solution scheme depends on the partial derivative of the necessary optimality conditions (44). An analytic expression for the corresponding square Jacobian can be stated as

$$\mathbf{H}(\mathbf{x}) = \mathbf{H}_1 + \lambda_1 \cdot \mathbf{H}_{\text{TV}}(\mathbf{x}) + \lambda_2 \cdot \mathbf{H}_{\text{W}}(\mathbf{x}) + \lambda_3 \cdot \mathbf{H}_{\text{Mb}} \quad , \quad (63)$$

where the individual derivatives are constant point matrices except for the derivatives of the regularizing terms that result from the consideration of the sparsity pattern of the MRI data in terms of the finite difference and Wavelet transformations. In detail, the individual derivatives associated with the summands in (44) are given by

$$\mathbf{H}_1 = \frac{\partial \mathbf{f}_1(\mathbf{x})}{\partial \mathbf{x}} = (\mathbf{M}_s \cdot (\mathbf{W}_2 \otimes \mathbf{W}_1)^*)^T \cdot (\mathbf{M}_s \cdot (\mathbf{W}_2 \otimes \mathbf{W}_1)) \quad (64)$$

for the fundamental quadratic cost function — which is identical to

$$\mathbf{H}_1 = \mathcal{M}_s^H \cdot \mathcal{M}_s \quad (65)$$

according to the definition of \mathcal{M}_s in (34) —

$$\mathbf{H}_\iota(\mathbf{x}) = \frac{\partial \mathbf{f}_\iota(\mathbf{x})}{\partial \mathbf{x}} = \frac{\Psi_\iota^{*T} \cdot \Psi_\iota}{2Q_\iota(\mathbf{x})} - \frac{\left(\Psi_\iota^{*T} \cdot \Psi_\iota \cdot \mathbf{x} \right) \cdot \left(\Psi_\iota^{*T} \cdot \Psi_\iota \cdot \mathbf{x} \right)^H}{4Q_\iota^3(\mathbf{x})} \quad (66)$$

for the regularizing terms $\iota \in \{\text{TV}, \text{W}\}$, and

$$\mathbf{H}_{\text{Mb}} = \frac{\partial \mathbf{f}_{\text{Mb}}(\mathbf{x})}{\partial \mathbf{x}} = \text{diag} \{ \text{col}(\mathbf{E} - \mathbf{M}_b) \} = \mathcal{M}_b \quad . \quad (67)$$

In analogy to the linearized solution procedure presented in the previous subsection, the range bounds introduced in (59)–(61) can be used to minimize the effect of overestimation in an interval evaluation of (66). For that purpose, the following interval expressions

$$\mathbf{H}_\iota([\mathbf{x}]) = \frac{1}{4Q_\iota([\mathbf{x}])} \cdot \Psi_\iota^{*T} \cdot \left(2 \cdot \mathbf{I}_{m \cdot n} - \left(\check{\mathbf{f}}_\iota([\mathbf{x}]) \right) \cdot \left(\check{\mathbf{f}}_\iota([\mathbf{x}^*]) \right)^T \right) \cdot \Psi_\iota \quad (68)$$

can be employed during the evaluation of the Krawczyk iteration (62).

Moreover, the iteration (62) depends on the matrix \mathbf{Y}_H which is defined as the (approximate) inverse of the Jacobian (63) according to

$$\mathbf{Y}_H = \left(\mathbf{H}(\mathbf{x}_m) \right)^{-1} \quad (69)$$

after its evaluation at the midpoint

$$\mathbf{x}_m = \text{mid} \{ [\mathbf{x}] \} \quad (70)$$

of the current interval enclosure of the desired reconstructed image. In analogy to the simplified procedure, this term can be approximated by means of the Neumann series (in the case of its convergence), which leads to

$$\mathbf{Y}_H \approx 2 \cdot \mathbf{I}_{m \cdot n} - \mathbf{H}(\mathbf{x}_m) . \quad (71)$$

If this series expansion does not converge, the matrix $\mathbf{H}(\mathbf{x}_m)$ needs to be inverted in classical floating-point arithmetic.

In contrast to the procedure from the previous subsection, the iteration (62) is not influenced by possible inaccuracies due to the approximation of the matrix \mathbf{Y}_H as long as the norm of the matrix $\mathbf{I} - \mathbf{Y}_H \cdot \mathbf{H}([\mathbf{x}])$ is sufficiently small. This matrix captures all arising approximation and truncation errors in a rigorous manner during the evaluation of the iteration formula (62).

The Krawczyk iteration (62) is initialized with the exact interval enclosure $[\mathbf{x}] = [\mathbf{x}]_{\text{ini}}$ of the simplified optimization problem

$$\tilde{\mathbf{f}}(\mathbf{x}) = \mathbf{f}_1(\mathbf{x}) + \lambda_3 \cdot \mathbf{f}_{\text{Mb}}(\mathbf{x}) = \mathbf{0} , \quad (72)$$

resulting from the parameter choice $\lambda_1 = \lambda_2 = 0$ in (44) for all possible measured data $\mathbf{y}' \in [\mathbf{y}']$. This simplified solution can be stated explicitly with the help of (65) and (67) in terms of

$$[\mathbf{x}]_{\text{ini}} = \left(\mathcal{M}_s^H \cdot \mathcal{M}_s + \lambda_3 \cdot \mathcal{M}_b \right)^{-1} \cdot \mathcal{M}_s^H \cdot [\mathbf{y}'] \quad (73)$$

and is, therefore, identical to the initialization $[\mathbf{x}]^{(0)}$ of the simplified iteration scheme (54).

Now, the following three cases need to be distinguished [12, 13, 16, 18]:

Case 1: The initialization interval $[\mathbf{x}]_{\text{ini}}$ does not contain any possible solution of the full optimization problem (44) if the evaluation of (62), leading to the vector $[\mathbf{k}]$, and the corresponding initialization for $[\mathbf{x}] = [\mathbf{x}]_{\text{ini}}$ do not overlap according to

$$[\mathbf{k}] \cap [\mathbf{x}]_{\text{ini}} = \emptyset . \quad (74)$$

Then, the initial search domain needs to be enlarged. Commonly, the enlargement is performed by the convex hull over each element of both interval vectors $[\mathbf{k}]$ and $[\mathbf{x}]_{\text{ini}}$ according to

$$[\mathbf{x}]_{\text{ini}} := [\mathbf{k}] \cup [\mathbf{x}]_{\text{ini}} . \quad (75)$$

To find a solution, the iteration (62) is then restarted with the redefined, inflated interval box $[\mathbf{x}]_{\text{ini}}$.

Case 2: If a partial overlapping between the initialization $[\mathbf{x}]_{\text{ini}}$ as well as with the interval box $[\mathbf{k}]$ occurs according to

$$[\mathbf{k}] \not\subset [\mathbf{x}]_{\text{ini}} \quad \text{with} \quad [\mathbf{k}] \cap [\mathbf{x}]_{\text{ini}} \neq \emptyset , \quad (76)$$

the same inflation of the solution domain as in (75) is performed. Finally, assuming convergence of the Krawczyk iteration, the following **Case 3** will be obtained.

Case 3: The interval domain $[\mathbf{x}]$, and thus also $[\mathbf{k}]$, is guaranteed to contain the solution of the optimization problem (44) if the relation

$$[\mathbf{k}] \subset [\mathbf{x}] \quad (77)$$

holds for all vector components of $[\mathbf{x}]$. The iteration according to this last case is continued after improving the interval enclosure according to the refined set

$$[\mathbf{x}] := [\mathbf{k}] \cap [\mathbf{x}] \quad (78)$$

up to the point where the difference of the interval diameters between $[\mathbf{x}]$ and $[\mathbf{k}]$ falls below some predefined threshold value.

5 Numerical Results

For the computation of interval bounds² for fluid flow rates from the reconstructed images $[\mathbf{x}]$ according to (57), it is necessary to evaluate the corresponding phase angles in an element-wise manner for each entry $[X_{ij}]$, $i \in \{1, \dots, m\}$, $j \in \{1, \dots, n\}$, in the associated matrix $[\mathbf{X}]$, cf. (1).

This is done by a generalization of the `atan2` function to a four-quadrant definition according to Tab. 1. The definitions in this table are based on the assumptions that the cases 13, 14, and 16 (corresponding to the principal values of the arc-tangent function) are evaluated directly on the basis of the `atan` implementation available in the interval toolbox `INTLAB` [23] for `MATLAB`.

²In the following, interval quantities are specified by their lower and upper bounds (resp. their infima and suprema) according to $[x_R] = [\inf\{[x_R]\} ; \sup\{[x_R]\}]$ and $[x_I] = [\inf\{[x_I]\} ; \sup\{[x_I]\}]$.

Table 1: Interval-based computation of phase angles $\phi \in [\inf\{\phi\}; \sup\{\phi\}]$ for the complex interval data $[x_R] + j \cdot [x_I]$ as a set-valued generalization of the `atan2` function.

| case | $\inf\{[x_R]\}$ | $\sup\{[x_R]\}$ | $\inf\{[x_I]\}$ | $\sup\{[x_I]\}$ | $\inf\{\phi\}$ | $\sup\{\phi\}$ |
|------|-----------------|-----------------|-----------------|-----------------|---|---|
| 1 | < 0 | < 0 | < 0 | < 0 | $\arctan\left(\frac{\sup\{[x_I]\}}{\inf\{[x_R]\}}\right) - \pi$ | $\arctan\left(\frac{\inf\{[x_I]\}}{\sup\{[x_R]\}}\right) - \pi$ |
| 2 | < 0 | < 0 | < 0 | ≥ 0 | $-\pi$ | π |
| 3 | < 0 | < 0 | ≥ 0 | < 0 | N/A | N/A |
| 4 | < 0 | < 0 | ≥ 0 | ≥ 0 | $\arctan\left(\frac{\sup\{[x_I]\}}{\sup\{[x_R]\}}\right) + \pi$ | $\arctan\left(\frac{\inf\{[x_I]\}}{\inf\{[x_R]\}}\right) + \pi$ |
| 5 | < 0 | ≥ 0 | < 0 | < 0 | $\arctan\left(\frac{\sup\{[x_I]\}}{\inf\{[x_R]\}}\right) - \pi$ | $\arctan\left(\frac{\sup\{[x_I]\}}{\sup\{[x_R]\}}\right)$ |
| 6 | < 0 | ≥ 0 | < 0 | ≥ 0 | $-\pi$ | π |
| 7 | < 0 | ≥ 0 | ≥ 0 | < 0 | N/A | N/A |
| 8 | < 0 | ≥ 0 | ≥ 0 | ≥ 0 | $\arctan\left(\frac{\inf\{[x_I]\}}{\sup\{[x_R]\}}\right)$ | $\arctan\left(\frac{\inf\{[x_I]\}}{\inf\{[x_R]\}}\right) + \pi$ |
| 9 | ≥ 0 | < 0 | < 0 | < 0 | N/A | N/A |
| 10 | ≥ 0 | < 0 | < 0 | ≥ 0 | N/A | N/A |
| 11 | ≥ 0 | < 0 | ≥ 0 | < 0 | N/A | N/A |
| 12 | ≥ 0 | < 0 | ≥ 0 | ≥ 0 | N/A | N/A |
| 13 | ≥ 0 | ≥ 0 | < 0 | < 0 | $\inf\left\{\arctan\left(\frac{[x_I]}{[x_R]}\right)\right\}$ | $\sup\left\{\arctan\left(\frac{[x_I]}{[x_R]}\right)\right\}$ |
| 14 | ≥ 0 | ≥ 0 | < 0 | ≥ 0 | $\inf\left\{\arctan\left(\frac{[x_I]}{[x_R]}\right)\right\}$ | $\sup\left\{\arctan\left(\frac{[x_I]}{[x_R]}\right)\right\}$ |
| 15 | ≥ 0 | ≥ 0 | ≥ 0 | < 0 | N/A | N/A |
| 16 | ≥ 0 | ≥ 0 | ≥ 0 | ≥ 0 | $\inf\left\{\arctan\left(\frac{[x_I]}{[x_R]}\right)\right\}$ | $\sup\left\{\arctan\left(\frac{[x_I]}{[x_R]}\right)\right\}$ |

For all other cases, it was assumed that the origin of the complex plane as a point value has the phase value zero, while each complex interval $[X_{ij}]$ intersecting with the negative real axis provides the phase interval $[-\pi; \pi]$. Cases which are not explicitly listed (such as the positive, respectively, negative imaginary axes) are associated directly with the corresponding point-valued phases of $\pm \frac{\pi}{2}$. In addition, all cases further denoted by N/A are undefined due to improper interval definitions. For the remaining cases in Tab. 1, it is assumed implicitly that $\inf\{[x_R]\} \leq \sup\{[x_R]\}$ as well as $\inf\{[x_I]\} \leq \sup\{[x_I]\}$ as the characterization for a proper interval holds under all circumstances.

5.1 Description of the MRI Experiment: Local Optimization Approaches for the Reconstruction of Flow Rates from Measurements in Floating Point Representation

For the investigation of the interval-based evaluation technique for the image reconstruction, the following MRI experiment has been employed. It is based on ten repetitions of single point measurements in the k -space for the fluid flow in a circular-shaped pipe under consideration of a single cross section plane. These ten repetitions were repeated for different sampling percentages. As shown in Fig. 2, these percentages range from 10%–100%. The largest value corresponds to the task of an image reconstruction from fully sampled k -space information, while the smallest value represents the scenario in which only 10% of the data were acquired.

For each of these experiments, the phase information was then reconstructed by applying a conjugate gradient method as a local search procedure for the optimal data $[\mathbf{X}] \in \mathbb{C}^{m \times n}$, where $m = n = 64$ holds for the scenario under investigation. The extended cost function (36) was parameterized with the settings $\lambda_1 = 10^{-3}$, $\lambda_2 = 0$, and $\lambda_3 = 0.01$ with $\mu_{TV} = 10^{-6}$. The conjugate gradient method was evaluated for at most 200 iterations, where in each of them a maximum number of 150 line search steps was allowed with an accuracy threshold of 10^{-29} [19].

In Tab. 2, the columns *minimum* and *maximum* denote the extremal values of the flow rate computed by means of eq. (4) within the 10 repetitions of the measurement of each sampling percentage³. For the corresponding individual image reconstructions, mean values as well as respective empirical standard deviations were determined according to the two subsequent columns. It can be noticed that both extremal values for the fluid flow are well explained by the mean and standard deviation, which gives raise to the assumption that the measurement was not corrupted by any extreme outliers.

In preparation for the following subsection, where the influence of uncertainty in the k -space data was investigated, also a further reconstruction was performed, see the last column in Tab. 2. Here, the raw data in the k -space were first averaged in

³Note, all presented solution techniques (i.e., the classical floating point-based local optimization as well as the novel interval-based solution techniques) provide local velocity distributions for the velocity within a given ROI which are subsequently reduced to a flow rate value as scalar output quantity as an integral characterization of the fluidic properties in the pipe cross section under investigation.

a point-wise manner, while the image reconstruction was performed afterwards for the *averaged* data set. It can be seen that these values partially lead to significantly smaller and/or larger values for the reconstructed minimum and maximum bounds of the flow rate determined according to the previously describe procedure. Hence, it is practically reasonable to perform the image reconstruction separately for all available data sets as soon as multiple measurements have been performed for the same layer of a quasi-stationary fluid flow.

Table 2: Reconstruction of the absolute values of the flow rate in liters per minute on the basis of a floating point conjugate gradient method with 10 repetitions of the measurement.

| sampling | minimum | maximum | mean | std. dev. | averaged |
|----------|---------|---------|--------|-----------|----------|
| 100% | 38.229 | 46.390 | 43.028 | 2.828 | 46.683 |
| 90% | 37.538 | 44.073 | 41.643 | 2.043 | 45.797 |
| 80% | 37.348 | 43.262 | 40.755 | 2.296 | 45.851 |
| 70% | 36.481 | 43.203 | 40.544 | 2.218 | 47.390 |
| 60% | 39.270 | 44.832 | 42.564 | 1.953 | 48.590 |
| 50% | 39.103 | 43.134 | 40.749 | 1.230 | 43.215 |
| 40% | 36.211 | 46.764 | 42.397 | 3.382 | 42.916 |
| 30% | 36.921 | 43.547 | 41.587 | 1.950 | 48.107 |
| 20% | 38.476 | 44.131 | 41.173 | 2.235 | 44.658 |
| 10% | 44.810 | 47.748 | 46.124 | 0.973 | 38.704 |

Due to the fact that the evaluation of the first row in Tab. 2 is based on a fully sampled data set, it can be viewed as a reference measurement with which consistency of all further results can be checked experimentally. A graphical summary of these data is given in Fig. 1, where the horizontal dashed lines highlight the range of flow rates with 100% sampling and the gray bars the respective ranges of all other data sets. The black error bars indicate intervals centered around the mean values given in Tab. 2 with positive and negative deviations given by the computed standard deviations for each of the investigated sampling percentages.

5.2 Interval-Based Iterative Solution of Optimality Criteria: Validation of the Accuracy of the Approximations Involved in the Linearized Solution Approach

To analyze the sensitivity as well as the effectiveness of the suggested interval approach for the velocity reconstruction in compressed sensing in terms of the resulting interval diameters and its computational complexity, two different types of uncertainty models were compared. The first one exploits the averaged k -space information (see the last column of Tab. 2), which was inflated by independent interval uncertainty of either $\eta_{\%} \in \{0.01\%, 0.1\%, 1\%, 3\%\}$ of each data point.

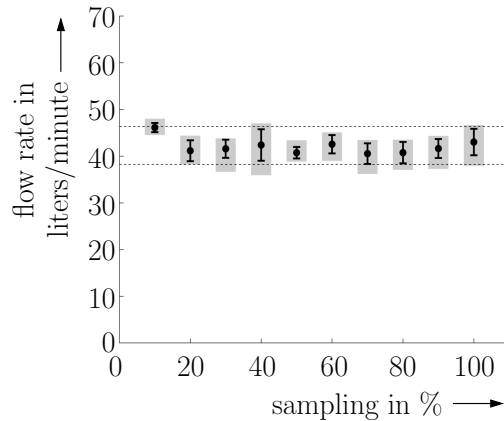


Figure 1: Visualization of the flow rate reconstruction using the floating point conjugate gradient approach.

It can be seen from Tab. 3 that an increase in the considered uncertainty leads to a two-sided growth of both interval bounds for the reconstructed flow rate. Here, table entries highlighted with a gray color denote those interval bounds that are wider than the worst-case reconstruction results from the before-mentioned point-valued conjugate gradient method.

Besides the possibility for a direct calculation of flow rates from the reconstructed velocity data including the influence of bounded uncertainty, it should be noted that the considered implementation of the proposed interval routine is computationally efficient in the sense that for uncertainties in the range⁴ of $\eta_{\%} \in \{0.01\%, 0.1\%, 1\%, 3\%\}$ the average computing time increased by a factor of approx. 5.5 in comparison to a single run of the conjugate gradient method. Only for tiny interval bounds in the case of $\eta_{\%} = 0.01\%$ uncertainty, the relative computing time increased by a factor of approx. 50. However, even the latter increase is by far less than considering multiple evaluations of the conjugate gradient approach with random disturbances of the k -space data, where even $m \times n = 4096$ evaluations for the extremal values of the data set do not provide any guarantee of

⁴Note, the two interval models presented in this section for an uncertainty representation are basically chosen as a starting point for the analysis of the sensitivity and reliability of a velocity reconstruction on the basis of variable sampling percentages. These intervals do not necessarily capture the complete ranges of random disturbances and measurement outliers occurring during the experiment. Future work will, therefore, deal with the systematic identification of the most appropriate disturbance models, for example by accounting for independent tolerance bounds with identical width for each measured point in the k -space with a simultaneous optimization of the respective bounds on the basis of various experiments. This future work will also deal with answering the question on whether or how the interval-based solution can be used to quantify image distortions during the sparsity-enforcing reconstruction which may be introduced by a random undersampling if — unfavorably — data points with high relevance are excluded from the measured data set.

including the complete range of possible reconstruction results.

Table 3: Interval-based reconstruction of the flow rate in liters per minute for various percentages of the assumed measurement uncertainty. Negative infima of the given values denote cases in which the uncertainty becomes too large to determine whether a flow rate in positive or negative direction takes place, cf. the interval diameters of 2π in the last row of Fig. 4.

| samp. | $\eta_{\%} = 0.01\%$ | | $\eta_{\%} = 0.1\%$ | | $\eta_{\%} = 1\%$ | | $\eta_{\%} = 3\%$ | |
|-------|----------------------|--------|---------------------|--------|-------------------|--------|-------------------|--------|
| | inf | sup | inf | sup | inf | sup | inf | sup |
| 100% | 42.364 | 43.909 | 33.840 | 50.497 | -65.912 | 91.102 | -93.241 | 93.241 |
| 90% | 44.866 | 46.144 | 37.414 | 52.593 | -75.868 | 91.958 | -93.241 | 93.241 |
| 80% | 42.541 | 43.803 | 34.659 | 51.028 | -37.342 | 84.316 | -93.241 | 93.241 |
| 70% | 46.290 | 48.173 | 34.738 | 57.355 | -19.203 | 82.081 | -93.241 | 93.241 |
| 60% | 44.274 | 46.043 | 35.567 | 53.963 | -31.317 | 83.051 | -93.241 | 93.241 |
| 50% | 40.306 | 47.534 | 37.015 | 50.439 | -17.240 | 76.605 | -93.241 | 93.241 |
| 40% | 36.700 | 50.049 | 33.465 | 52.790 | -17.769 | 80.482 | -93.241 | 93.241 |
| 30% | 39.563 | 51.834 | 30.103 | 60.619 | -47.507 | 90.212 | -93.241 | 93.241 |
| 20% | 39.059 | 39.539 | 36.551 | 41.887 | 4.005 | 64.139 | -41.996 | 84.861 |
| 10% | 37.555 | 38.453 | 37.082 | 38.904 | 34.450 | 41.159 | 17.804 | 56.076 |

To compare the outcome of the previous — simple — uncertainty model with an approach motivated by variations of the power spectral density (PSD) of each point in the k -space data, the following results in Tab. 4 are presented. Here, the standard deviation of the PSD for each point in the raw data from the experiment described in the previous subsection was computed first. For each of the sampling percentages, these standard deviations (defined for each individual point in the k -space) were normalized by the computed maximum value in a second stage (separately for the real and imaginary parts of the data set). Finally, additive complex-valued symmetric interval bounds were created from these quantities for each k -space point by scaling with the interval $[-\eta_{\text{PSD}} ; \eta_{\text{PSD}}]$, where η_{PSD} was chosen from the set $\eta_{\text{PSD}} \in \{0.01; 0.1; 1; 3\}$.

A comparison of Tabs. 3 and 4 shows that both uncertainty models provide quite similar results and justify the use of set-valued uncertainties with a constant percentage for each of the measurement points in the k -space, especially in cases of a sampling of more than 30 % of the points in the k -space.

This result is confirmed by Fig. 2, where the outcome of the classical conjugate gradient approach in gray bars is compared with both interval-based uncertainty models for the tolerance settings of $\eta_{\%} = 0.1\%$ and $\eta_{\text{PSD}} = 0.1$, respectively. It can be seen that the interval approach is able to predict the range of flow rates reliably (if compared with the dashed lines that are identical to Fig. 1), except for the case of 10 % sampling in which also the classical technique fails to provide estimates that are consistent with the fully sampled setting. Most likely, the reason for this phenomenon is the fact that parts of the relevant data points were not captured sufficiently within the measurement process. In addition, it should be pointed out

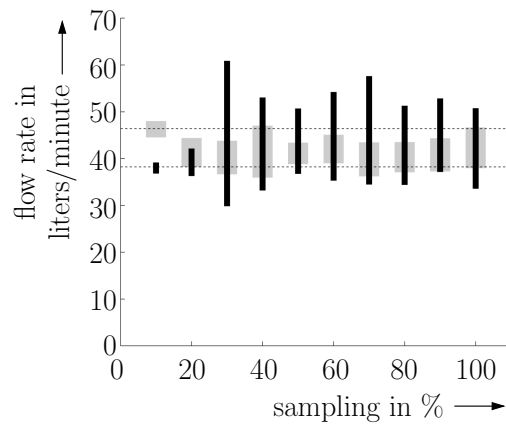
Table 4: Interval-based reconstruction of the flow rate in liters per minute for various uncertainty levels η_{PSD} derived from variations of the power spectral density.

| samp. | $\eta_{\text{PSD}} = 0.01$ | | $\eta_{\text{PSD}} = 0.1$ | | $\eta_{\text{PSD}} = 1$ | | $\eta_{\text{PSD}} = 3$ | |
|-------|----------------------------|--------|---------------------------|--------|-------------------------|--------|-------------------------|--------|
| | inf | sup | inf | sup | inf | sup | inf | sup |
| 100% | 42.488 | 43.790 | 35.543 | 49.193 | -46.386 | 87.237 | -93.241 | 93.241 |
| 90% | 44.992 | 46.020 | 39.331 | 51.075 | -55.045 | 89.023 | -93.241 | 93.241 |
| 80% | 42.570 | 43.774 | 35.183 | 50.602 | -33.069 | 83.193 | -93.241 | 93.241 |
| 70% | 46.192 | 48.273 | 35.603 | 56.639 | -29.974 | 85.053 | -93.241 | 93.241 |
| 60% | 44.249 | 46.070 | 34.932 | 54.467 | -36.030 | 84.175 | -93.241 | 93.241 |
| 50% | 39.366 | 48.390 | 34.688 | 52.120 | -53.283 | 88.013 | -93.241 | 93.241 |
| 40% | 30.214 | 55.176 | 27.438 | 57.047 | -85.971 | 92.974 | -93.241 | 93.241 |
| 30% | 36.986 | 54.422 | 22.055 | 66.554 | -92.272 | 93.232 | -93.241 | 93.241 |
| 20% | 35.943 | 42.359 | 3.081 | 64.875 | -93.241 | 93.241 | -93.241 | 93.241 |
| 10% | 36.721 | 39.238 | 29.906 | 44.293 | -93.241 | 93.241 | -93.241 | 93.241 |

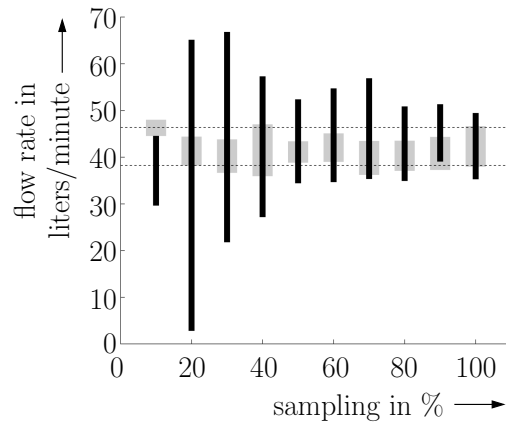
that the computed interval ranges are typically wider than the floating point results because independent uncertainty was considered for each available k -space point in comparison with the classical approach in which only ten repetitions of the whole measurement were used in order to quantify the range of possible flow rates.

Finally, a graphical comparison of the influence of different interval diameters of the uncertainties can be found in Figs. 3 and 4. Here, the first rows depict the spatial dependency of the reconstructed flow rates which are directly proportional to the computed phase angles. The second rows, which are point-wise strictly larger than the infima, represent the corresponding upper interval bounds, while the third rows visualize the increase of the local uncertainty distribution for variable values of $\eta_{\%}$. Note that the circular geometry of the pipe under investigation can be seen directly in those figures by the point values zero in the respective outer domains.

Figs. 3 and 4 highlight especially the fact that the uncertainty distribution in the reconstructed images is not homogeneous over all volume elements and that excessively large measurement uncertainty leads to the phenomenon that phases can no longer be reconstructed due to the fact that entries in the interval matrix $[\mathbf{X}]$ intersect with the negative real axis in the complex plane (i.e., angle bounds become equal to $[-\pi ; \pi]$). Comparing the outcome of the interval-based velocity reconstruction with the uncertainty of a scalar volume flow variable as shown in Fig. 1, it should be pointed out that Fig. 1 only allows for detecting significant variations of the averaged flow rate over the complete pipe cross section (on the basis of multiple measurements), while the interval approach allows for determining directly those locations in the reconstructed image where the computed results are most sensitive against the assumed error (resp. disturbance) model.



(a) Flow rates corresponding to $\eta\% = 0.1\%$ in Tab. 3.



(b) Flow rates corresponding to $\eta_{PSD} = 0.1$ in Tab. 4.

Figure 2: Visualization of the interval-based flow rates reconstruction in comparison with the floating point conjugate gradient approach.

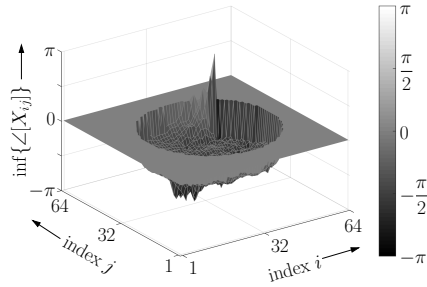
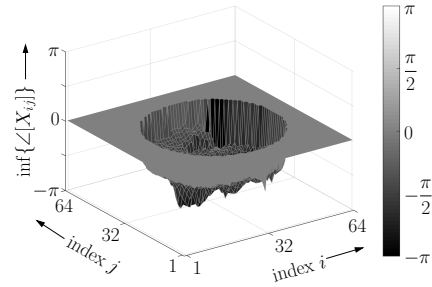
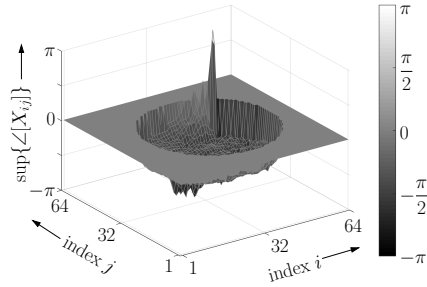
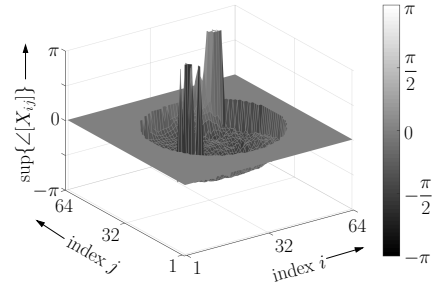
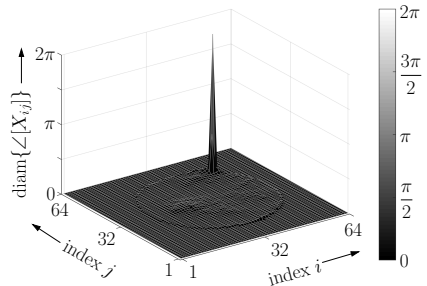
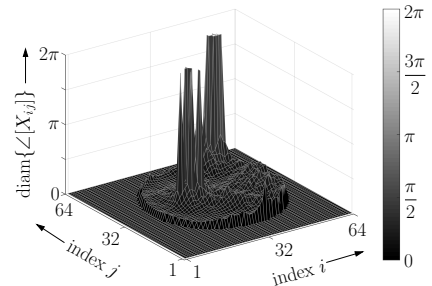
(a) Lower interval bound $\inf\{\angle[\mathbf{X}]\}$.(b) Lower interval bound $\inf\{\angle[\mathbf{X}]\}$.(c) Upper interval bound $\sup\{\angle[\mathbf{X}]\}$.(d) Upper interval bound $\sup\{\angle[\mathbf{X}]\}$.(e) Interval diameter $\text{diam}\{\angle[\mathbf{X}]\}$.(f) Interval diameter $\text{diam}\{\angle[\mathbf{X}]\}$.

Figure 3: Comparison of the interval enclosures for the reconstructed phase angles $\angle[\mathbf{X}]$ with the uncertainty levels $\eta\% = 0.01\%$ (left column) and $\eta\% = 0.1\%$ (right column) according to Tab. 3 and 60% sampling.

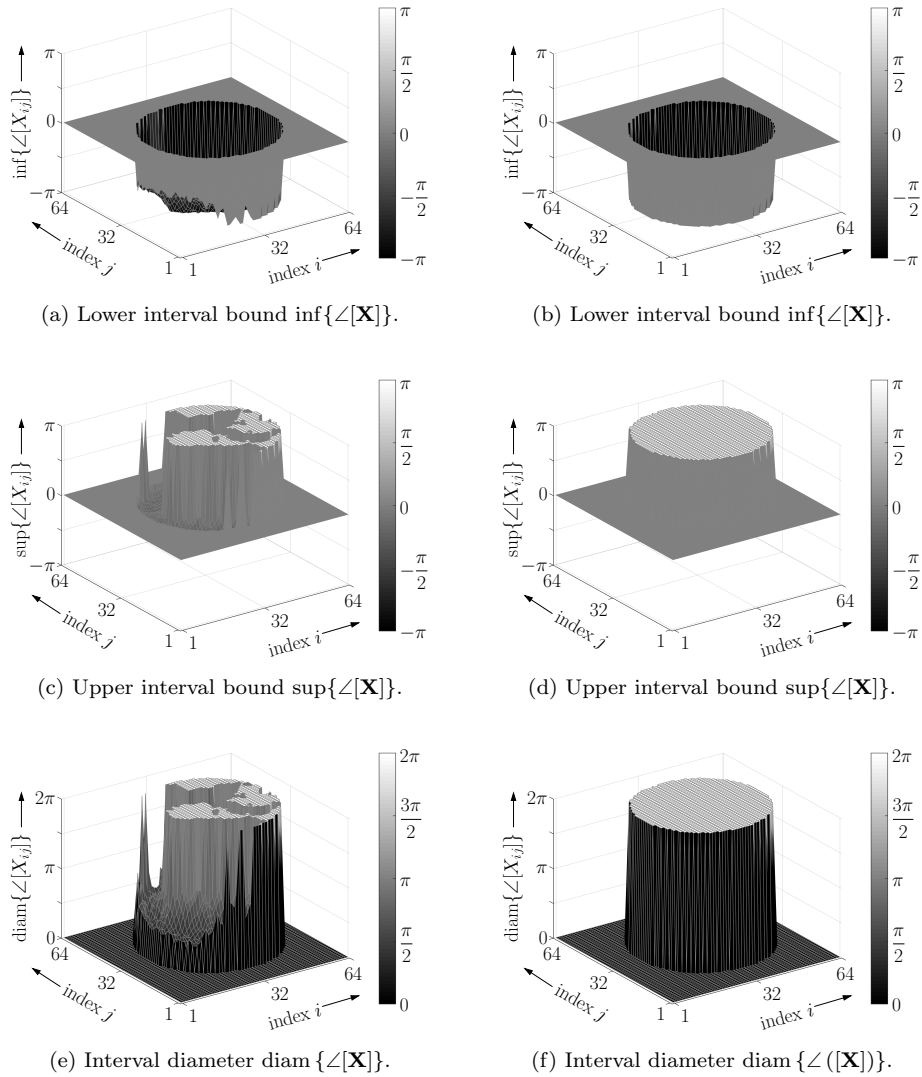


Figure 4: Comparison of the interval enclosures for the reconstructed phase angles $\angle[\mathbf{X}]$ with the uncertainty levels $\eta\% = 1\%$ (left column) and $\eta\% = 3\%$ (right column) according to Tab. 3 and 60% sampling.

6 Conclusions and Outlook on Future Work

In this paper, a novel technique has been derived for the interval-based analysis of the influence of measurement uncertainty in the frame of compressed sensing techniques for MRI. On the one hand, it allows for a direct computation of interval bounds for the reconstructed spatial distribution of velocity data as well as for the respective (integral) flow rates. On the other hand, it could be shown that simple uncertainty models (based on independent uncertainties for each individual measurement point in the k -space) can be treated in a numerically efficient manner. These techniques typically only increase the computational effort by a factor smaller than 10 which is by at least two orders of magnitude smaller than the effort that would be necessary for an uncertainty quantification on the basis of brute force Monte-Carlo techniques.

In future work, a thorough comparison will be performed between the proposed linearized evaluation technique as well as a fully verified variant of the interval Newton method for solving the necessary optimality criteria related to the cost function $J(\mathbf{x})$ derived in this paper. A first attempt concerning this comparison can be found in [22]. Both interval-based evaluation techniques will, furthermore, be employed to optimize the sampling patterns in the k -space to find solutions which allow for an accelerated MRI measurement as well as for a further systematic reduction of reconstruction uncertainty. In addition, also the identification of most appropriate interval representations of the employed uncertainty models is a subject of ongoing research.

References

- [1] Bouboulis, P. Wirtinger's Calculus in General Hilbert Spaces. *arXiv e-prints*, page arXiv:1005.5170, May 2010.
- [2] Brown, R.W., Cheng, Y.-Ch.N., Haacke, E.M., Thompson, M.R., and Venkatesan, R. *Magnetic Resonance Imaging: Physical Principles and Sequence Design*, volume 82. Wiley-Liss New York:, 1999. DOI: 10.1002/9781118633953.
- [3] Bruschewski, M., Freudenhammer, D., Buchenberg, W.B., Schiffer, H.-P., and Grundmann, S. Estimation of the Measurement Uncertainty in Magnetic Resonance Velocimetry Based on Statistical Models. *Experiments in Fluids*, 57(5):83, 2016. DOI: 10.1007/s00348-016-2163-3.
- [4] Bruschewski, M., Kolkman, H., John, K., and Grundmann, S. Phase-Contrast Single-Point Imaging with Synchronized Encoding: A More Reliable Technique for in Vitro Flow Quantification. *Magnetic resonance in medicine*, 81(5):2937–2946, 2019. DOI: 10.1002/mrm.27604.
- [5] Candés, E.J., Romberg, J.K., and Tao, T. Stable Signal Recovery from Incomplete and Inaccurate Measurements. *Communications on Pure and Ap-*

- plied Mathematics: A Journal Issued by the Courant Institute of Mathematical Sciences*, 59(8):1207–1223, 2006. DOI: 10.1002/cpa.20124.
- [6] Donoho, D.L. Compressed Sensing. *IEEE Transactions on Information Theory*, 52(4):1289–1306, 2006. DOI: 10.1109/TIT.2006.871582.
- [7] Elkins, C.J. and Alley, M.T. Magnetic Resonance Velocimetry: Applications of Magnetic Resonance Imaging in the Measurement of Fluid Motion. *Experiments in Fluids*, 43(6):823–858, 2007. DOI: 10.1007/s00348-007-0383-2.
- [8] Fischer, R.F.H. *Precoding and Signal Shaping for Digital Transmission*. John Wiley & Sons, Inc, New York, 2002. DOI: 10.1002/0471439002.
- [9] Gentleman, W.M. Matrix Multiplication and Fast Fourier Transforms. *Bell System Technical Journal*, 47, 07 1968. DOI: 10.1002/j.1538-7305.1968.tb00074.x.
- [10] Holland, D.J., Malioutov, D.M., Blake, A., Sederman, A.J., and Gladden, L.F. Reducing Data Acquisition Times in Phase-Encoded Velocity Imaging Using Compressed Sensing. *Journal of magnetic resonance*, 203(2):236–246, 2010. DOI: 10.1016/j.jmr.2010.01.001.
- [11] Hrmander, L. *An Introduction to Complex Analysis in Several Variables*. North-Holland Mathematical Library, Volume 7. North-Holland Pub. Co, Amsterdam, 3 edition, 1990.
- [12] Jaulin, L., Kieffer, M., Didrit, O., and Walter, É. *Applied Interval Analysis*. Springer-Verlag, London, 2001. DOI: 10.1007/978-1-4471-0249-6.
- [13] Krawczyk, R. Newton-Algorithmen zur Bestimmung von Nullstellen mit Fehlerschranken. *Computing*, 4:189–201, 1969. DOI: 10.1007/BF02234767, In German.
- [14] Larson 3rd, T.C., Kelly, W.M., Ehman, R.L., and Wehrli, F.W. Spatial Misregistration of Vascular Flow During MR Imaging of the CNS: Cause and Clinical Significance. *AJR. American Journal of Roentgenology*, 155(5):1117–1124, 1990. DOI: 10.2214/ajr.155.5.2120946.
- [15] Lustig, M., Donoho, D., and Pauly, J.M. Sparse MRI: The Application of Compressed Sensing for Rapid MR Imaging. *Magnetic Resonance in Medicine: An Official Journal of the International Society for Magnetic Resonance in Medicine*, 58(6):1182–1195, 2007. DOI: 10.1002/mrm.21391.
- [16] Moore, R.E., Kearfott, R.B., and Cloud, M.J. *Introduction to Interval Analysis*. SIAM, Philadelphia, 2009. DOI: 10.1137/1.9780898717716.
- [17] Moran, P.R., Moran, R.A., and Karstaedt, N. Verification and Evaluation of Internal Flow and Motion. True Magnetic Resonance Imaging by the Phase Gradient Modulation Method. *Radiology*, 154(2):433–441, 1985. DOI: 10.1148/radiology.154.2.3966130.

- [18] Neumaier, A. *Interval Methods for Systems of Equations*. Cambridge University Press, Encyclopedia of Mathematics, Cambridge, 1990. DOI: 10.1017/CB09780511526473.
- [19] Nocedal, J. and Wright, S.J. *Numerical Optimization*. Springer-Verlag, New York, 2nd edition, 2006. DOI: 10.1007/978-0-387-40065-5.
- [20] Proakis, J.G. and Manolakis, D.G. *Digital Signal Processing: Principles, Algorithms, and Applications*. Prentice-Hall, Inc., Upper Saddle River, NJ, USA, 3 edition, 1996.
- [21] Rao, K.R. and Yip, P.C. *The Transform and Data Compression Handbook*. CRC Press Inc, Boca Raton, 2000. DOI: 10.1201/9781315220529.
- [22] Rauh, A., John, K., Bruschewski, M., and Grundmann, S. Comparison of Two Different Interval Techniques for Analyzing the Influence of Measurement Uncertainty in Compressed Sensing for Magnet Resonance Imaging. In *Proceedings of 18th European Control Conference ECC 2020*, St. Petersburg, Russia, 2020. Accepted.
- [23] Rump, S.M. INTLAB — INTerval LABoratory. In Csendes, T., editor, *Developments in Reliable Computing*, pages 77–104. Kluwer Academic Publishers, 1999.
- [24] Theilheimer, F. A Matrix Version of the Fast Fourier Transform. *IEEE Transactions on Audio and Electroacoustics*, 17:158–161, 07 1969. DOI: 10.1109/TAU.1969.1162031.
- [25] Weinmann, A. *Uncertain Models and Robust Control*. Springer-Verlag, Wien, 1991. DOI: 10.1007/978-3-7091-6711-3.